



**HAL**  
open science

# Elemental quantification and analysis of structural abnormalities in neurons from Parkinson's-diseased brains by X-ray fluorescence microscopy and diffraction

Karina Joppe, Jan-David Nicolas, Tilman Grünewald, Marina Eckermann,  
Tim Salditt, Paul Lingor

► **To cite this version:**

Karina Joppe, Jan-David Nicolas, Tilman Grünewald, Marina Eckermann, Tim Salditt, et al.. Elemental quantification and analysis of structural abnormalities in neurons from Parkinson's-diseased brains by X-ray fluorescence microscopy and diffraction. *Biomedical optics express*, 2020, 11 (7), pp.3423-3443. 10.1364/BOE.389408 . hal-03139973

**HAL Id: hal-03139973**

**<https://amu.hal.science/hal-03139973>**

Submitted on 15 Jul 2022

**HAL** is a multi-disciplinary open access archive for the deposit and dissemination of scientific research documents, whether they are published or not. The documents may come from teaching and research institutions in France or abroad, or from public or private research centers.

L'archive ouverte pluridisciplinaire **HAL**, est destinée au dépôt et à la diffusion de documents scientifiques de niveau recherche, publiés ou non, émanant des établissements d'enseignement et de recherche français ou étrangers, des laboratoires publics ou privés.



# Elemental quantification and analysis of structural abnormalities in neurons from Parkinson's-diseased brains by X-ray fluorescence microscopy and diffraction

KARINA JOPPE,<sup>1,2,9</sup>  JAN-DAVID NICOLAS,<sup>3,9</sup> TILMAN A. GRÜNEWALD,<sup>4,5</sup> MARINA ECKERMANN,<sup>3</sup> TIM SALDITT,<sup>3,6</sup> AND PAUL LINGOR<sup>1,2,7,8,\*</sup>

<sup>1</sup>Department of Neurology, University Medical Center Goettingen, Robert-Koch-Straße 40, 37075 Goettingen, Germany

<sup>2</sup>Center for Biostructural Imaging of Neurodegeneration, University Medical Center Goettingen, Von-Siebold-Straße 3a, 37075 Goettingen, Germany

<sup>3</sup>Institute for X-Ray Physics, Georg-August-University Goettingen, Friedrich-Hund-Platz 1, 37077 Goettingen, Germany

<sup>4</sup>European Synchrotron Radiation Facility, 71 Avenue des Martyrs, 38043 Grenoble, France

<sup>5</sup>CNRS, Centrale Marseille, Institut Fresnel, Aix-Marseille University, 52 Avenue Escadrille Normandie Niemen, 13013 Marseille, France

<sup>6</sup>Cluster of Excellence "Multiscale Bioimaging: from Molecular Machines to Networks of Excitable Cells" (MBExC), University of Goettingen, Germany

<sup>7</sup>Department of Neurology, School of Medicine, University Hospital rechts der Isar, Technical University of Munich, Ismaninger Straße 22, 81675 Munich, Germany

<sup>8</sup>DFG Cluster of Excellence Nanoscale Microscopy and Molecular Physiology of the Brain (CNMPB), University Medical Center Göttingen, Robert-Koch-Str. 40, 37075 Göttingen, Germany

<sup>9</sup>These authors contributed equally

\*[paul.lingor@tum.de](mailto:paul.lingor@tum.de)

**Abstract:** In this work we use scanning X-ray microscopy to study the structure and elemental composition of neuromelanin-positive neurons in substantia nigra tissue of Parkinson patients (PD) and controls. A total of 53 neurons were analyzed with X-ray fluorescence (XRF) and diffraction using sub- $\mu\text{m}$ -focused synchrotron radiation. A statistical evaluation identified copper as the most group-discriminating element and indicated that interindividual and intraindividual variations are of great relevance in tissue measurements of diseased patients and prevent from automated group clustering. XRF analyses of two Lewy bodies (LBs) highlight a heterogeneity in elemental distributions in these LBs, whereas an innovative X-ray diffraction-based method approach was used to reveal  $\beta$ -sheet-rich crystalline structures in LBs. Overall, sub- $\mu\text{m}$ -focus X-ray microscopy highlighted the elemental heterogeneity in PD pathology.

© 2020 Optical Society of America under the terms of the [OSA Open Access Publishing Agreement](#)

## 1. Introduction

Parkinson's disease (PD) is the second most common neurodegenerative disease worldwide and, so far, no drugs are available for its prevention or causative treatment. PD is often only diagnosed when patients already show frequently occurring symptoms such as bradykinesia, resting tremor, rigidity or gait disturbances [1]. At this stage, it is assumed that pathological changes have already occurred, primarily within brain regions controlling motor function [2]. For a better understanding of PD pathology, biomarkers for accurate and early onset identification of the disease are needed.

Iron accumulation and  $\alpha$ -synuclein-containing Lewy bodies (LBs) are prominent neuropathological findings in PD. Using mass spectrometry, iron accumulation was pronounced within

the substantia nigra (SN) in PD patients compared to control patients [3]. Magnetic Resonance Imaging (MRI) studies showed that iron chelators reduced the iron content inside the SN of patients [4,5]. Using atomic absorption spectroscopy, an increased iron content was detected within the SN of Lewy Body disease (LBD) patients compared to Alzheimer's disease patients or controls [6]. Furthermore, histochemical analysis showed redox-active iron within LBs of PD patients [7]. Therefore, the interaction of  $\alpha$ -synuclein and iron is believed to foster disease development [8]. For example, increased levels of oxidative stress or generation of reactive oxygen species within the brain are thought to be partially iron-induced and mediate consequences such as protein aggregation [9].

Indeed, not only iron but also other trace elements such as copper, manganese, cobalt or aluminum were shown to cause  $\alpha$ -synuclein fibrillation *in vitro* [10]. Since  $\alpha$ -synuclein in form of fibrils is a major component of LBs, dyshomeostasis of trace elements and their interaction with  $\alpha$ -synuclein could play an important role in the pathogenesis of PD.

Earlier studies have quantified intra- and extracellular levels of trace elements in SN neurons by mass spectrometry, atomic absorption spectroscopy or electron probe microanalysis such as electron-dispersive X-ray (EDX) microanalysis [6,11,12]. In recent years, X-ray based techniques such as X-ray fluorescence (XRF) or scanning transmission X-ray microscopy (STXM) have joined the list of techniques for the microanalysis of neural cells and tissues [13,14]. XRF has already been used in studies related to the role of trace elements in redox regulation and signaling, see e.g. [13–16]. Similar to electron-based microanalysis, XRF can be used to map absolute trace elements concentrations with a sensitivity limit around 0.1  $\mu\text{g g}^{-1}$  to 1  $\mu\text{g g}^{-1}$  [17].

In addition to mapping the concentration of metal ions and trace elements, a structural characterization of the tissue can be realized by X-ray diffraction (XRD). By raster scanning of a tightly focused X-ray beam over the sample, the scattering signal can be recorded together with XRF generated in the sample, see e.g. [18–21]. The scattering signals have often been overlooked, despite the fact that they carry valuable information about the structure, especially when dealing with heterogeneous samples with local ordering. The scattering patterns can be post-processed to generate two-dimensional maps of a multitude of structural parameters, e.g. tissue density, short range order, presence of crystalline components, or orientation of neurons.

In a previous study on tissue sections from a single PD patient and one age-matched control [18], we quantified the elemental distribution of Fe, Cu, Zn and other trace elements and verified the well-established metal dyshomeostasis in the brain of PD patients. Although this pilot study demonstrated the versatility of X-ray-based microanalysis, no statistical information could be extracted due to a sample limitation of a single patient and control (CO).

In this study, we have further developed tissue analysis by XRD and XRF and have scanned a total of nine human brain samples (PD and CO) to quantify the elemental content in neuromelanin-pigmented neurons using a resolution in sub- $\mu\text{m}$  range and a higher photon energy which allowed us to measure further elements such as arsenic and selenium. Midbrain tissue containing parts of SN was used due to a known dyshomeostasis of several trace elements (Fe, Cu, Zn, Mn) in the SN of PD patients [3,22] and for comparability with our previous study. In total, the absolute concentration of 13 elements in 53 dopaminergic neurons was analyzed. This offers further insight into the elemental distribution within dopaminergic cells on the single cell level, complementing non-local, elementomic approaches in PD based on serum, plasma or cerebrospinal fluid (CSF) samples [23–27]. The advantage of a high spatial resolution in XRF is exploited to quantify element concentrations not only in cells but also in sub-cellular structures. In addition, we have evaluated the elemental composition within two LBs and analyzed the scattering signal which can be attributed to  $\beta$ -sheet-rich structures. This is, to our knowledge, the first time that XRF and XRD have been applied to characterize LBs in PD, extending the previously reported synchrotron-based x-ray spectroscopy of LBs [28]. For the purpose of this diffraction analysis, we introduce a model-independent approach of principal component analysis.

As detailed in the results and discussion section, our data indicate a pronounced heterogeneity of trace element concentrations in neuromelanin-positive neurons for different individuals. We finish the paper by conclusions concerning both the possible relevance of this heterogeneity for future improvements and recommendations in view of scaling the sample size.

## 2. Methods

### 2.1. Human midbrain tissue samples

Human brain samples were obtained from the UK Brain Bank (Parkinson's UK, London, England) as extracted midbrain tissue blocks. The samples were approved by the Multicenter Research Ethics Committee (07/MRE09/72). The patient demographics are summarized in Table 1. SN was identified by neuromelanin-positive cells. Analysis of  $\alpha$ -synuclein pathology and classification into Braak stages were provided by the UK Brain Bank.

**Table 1. Patient demographics. CO = control, PD = Parkinson's disease, LB = Lewy body, MS = multiple sclerosis, F = female, M = male, post-mortem interval = the time between death and tissue freezing, N/A = not available, y = years, h = hours.**

patient ID	patient group	analysis target	main diagnosis	age (y)	gender	$\alpha$ -synuclein pathology (Braak stage)	disease duration (y)	post mortem interval (h)
PD1	PD	cells	PD	82	F	6	14	18
PD2	PD	cells/ LB	PD	87	M	N/A	9	21
PD3	PD	cells	PD	73	M	6	19	10
PD4	PD	cells	PD	76	F	6	7	12
PD5	PD	LB	PD	76	M	6	7	15
CO1	CO	cells	cancer	75	M	N/A	N/A	24
CO2	CO	cells	cancer	60	F	N/A	N/A	13
CO3	CO	cells	cancer	89	F	N/A	N/A	13
CO4	CO	cells	MS	74	M	N/A	N/A	21

### 2.2. Sample preparation

Snap frozen midbrain blocks of four PD and four control patients were used for the X-ray analysis of native tissue sections. For the LB analysis, tissue sections from two PD patients were used (Fig. 1). In a cryostat (CM3050 S, Leica, Nussloch, Germany), tissue blocks were cut in 30  $\mu$ m thick sections using iron-free teflon-coated blades (DB80 LX, Nussloch) to avoid friction-induced particle contamination. Two adjacent sections were cut. The first section was mounted on a ring covered with Kapton foil (diameter 50 mm, Kapton 30  $\mu$ m thick), the second section was mounted on a polypropylene foil (PP)-covered ring (diameter 25 mm, PP 1  $\mu$ m thick). Sections on PP foil were dried at 60°C for 15 min. Another PP ring was put on top of each section and both rings covering one section were sealed with nail polish. The sections on Kapton rings were dried for 3 min at 60°C. The tissue was fixed with 100% methanol for 10 min at -20°C and kept at room temperature (RT) for immunohistochemical staining.

The sections on Kapton rings were used for  $\alpha$ -synuclein staining. Sections were rehydrated in Tris-buffered saline (TBS, Applichem) for 20 min. Afterwards, the sections underwent antigen retrieval in citrate buffer (Sigma-Aldrich) made with sodium citrate at pH 3 for 1 h at 60°C. After 30 min of cooling down, the sections were washed 3 $\times$ 5 min in TBS. Blocking was done in 5% normal goat serum (NGS, Cedarlane) in TBS with 0.1% Tween 20 (TBST, Applichem) for 1 h. Sections were incubated over night at 4°C with the first antibody (mouse anti- $\alpha$ -synuclein, LB509, Covance) diluted 1:250 in 5% NGS dissolved in TBS. On the next day, the sections

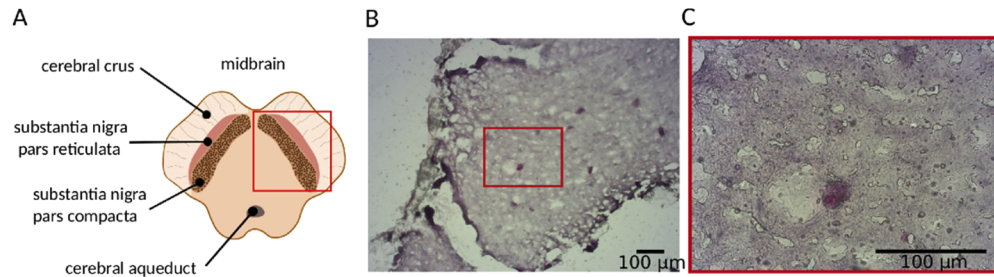


**Fig. 1.** Localization of LBs in human midbrain tissue. (A) Schematic anatomical representation of the SN. The red square indicates the region from where the available brain tissue originates. (B, C) Micrographs of different magnifications focus on a LB inside a neuromelanin-positive neuron of the SN. In order to identify LBs, human tissue was immunostained against  $\alpha$ -synuclein in an alkaline-phosphatase-coupled antibody staining. New fuchsin was used as a dye resulting in a red staining of the  $\alpha$ -synuclein-containing LB. Red squares are used to mark the position of the LB in lower magnifications.

were washed three times for 10 min each in TBS and were incubated with a secondary antibody conjugated with alkaline phosphatase (goat anti-mouse IgG/alkaline phosphatase, Dako) 1:150 in TBS for 45 min. Another washing step ( $3 \times 10$  min in TBS) followed. Adding Naphthol As-BI phosphate (Sigma-Aldrich) to the alkaline phosphatase, the fission product reacts with the added triphenylmethane dye new fuchsin (0.1 mg/ml; Sigma-Aldrich) and effects a red staining of  $\alpha$ -synuclein. After 20 min of incubation, the sections were washed for 5 min in  $H_2O$  and dried at RT. On the next day, the tissue was rehydrated in distilled  $H_2O$  for 5 min and incubated for 8 s in hemalum solution (Roth) to stain cell nuclei. After blueing of the samples for 10 min in  $H_2O$ , sections were dried at RT. Due to the yellow color of the Kapton foil, the hemalum staining of the sections deposited on Kapton was not visible in optical micrographs. Sections were covered with another Kapton ring and both rings were sealed with nail polish. An Axio Imager.Z2 microscope (Zeiss) was used to identify LB-like structures in PD tissue mounted on Kapton rings (Fig. 1(B,C)).

### 2.3. Experimental configuration

X-ray experiments were performed at the sub- $\mu$ m-focus experimental endstation (EH3) of beamline ID13 at the storage ring ESRF (Grenoble, France). The experimental configuration is sketched in Fig. 2.

The photon energy for the experiment was set to 14.8 keV with an energy spread of  $\Delta E/E = 0.1\%$  defined by a Si(111) channel-cut monochromator. To collect XRD data a two-dimensional single-photon counting X-ray detector (Eiger 4M, Dectris) was used. XRF photons were recorded using an energy-sensitive silicon-drift X-ray detector (Vortex EM, SII NanoTechnology Inc.). The detector distance of the XRD detector was calibrated using standard reference materials and the pyFAI-calib software [29]. The XRD detector distance and position of the primary beam (and detector tilt) was calibrated at distances  $z_{XRD} = \{303.194, 503.067, 901.188, 1298.137\}$  mm. During alignment, a list of possible detector distances was pre-calibrated and the multiple distances were used to verify the photon energy. For XRD measurements of LBs  $z_{XRD} = 303.194$  mm was used. The XRF detector was positioned, depending on the size of the sample holder, at two different distances,  $z_{XRF} = 25.5$  mm and 35.5 mm at a tilt angle  $\varphi$  of 15.6 degrees with respect to the X-ray beam, see Fig. 2. All other parameters relevant for fluorescence intensity calibration are summarized in Table 2.

X-ray focusing was achieved using two sets of sub- $\mu$ m-focusing Si compound refractive lenses, which generated a focal spot of  $240 \times 250$  nm<sup>2</sup> (horz.  $\times$  vert., cf. orientation in Fig. 2). The

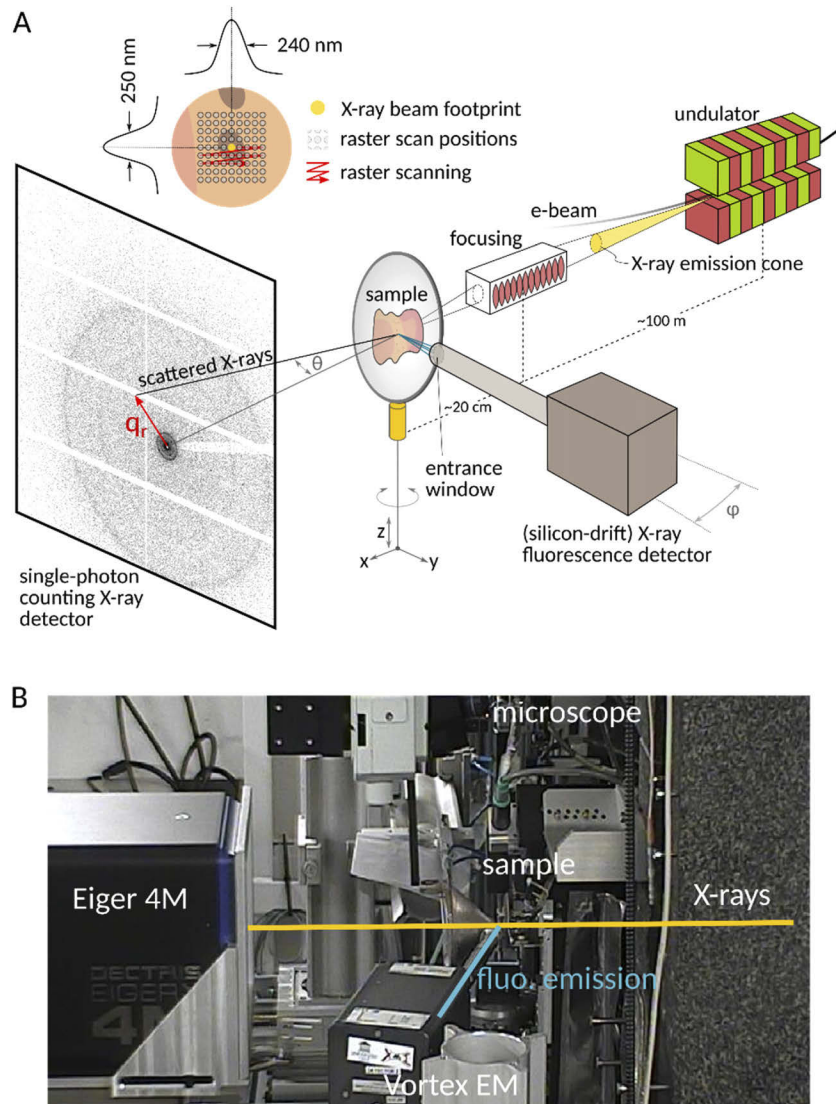


**Fig. 2.** Schematic drawing and photographs of the experiment setup and geometry. (A) X-rays are produced by oscillating electrons in an undulator. Besides other standard beamline optical components such as monochromatization, collimation or pre-focusing, X-rays are then focused using Si compound refractive lenses to produce a focal spot of  $240 \times 250 \text{ nm}^2$ . The sample is raster scanned through the focus of the X-ray beam. Scattered radiation is detected on an Eiger 4M single-photon counting pixel detector. Fluorescence radiation is detected with a Vortex EM silicon drift detector for energy-resolved photon detection. (B) Overview of the experimental setup with a mounted sample and all detectors in place. A helium-filled flighttube (omitted in A) is used to minimize air scattering and an attached beamstop blocks the (unscattered) primary beam from overexposing the sensitive pixel detector.

**Table 2. Configuration of the Vortex EM silicon drift detector. An aluminum cap with a circular aperture was placed on the detector as a collimator.**

Parameter	Value
Sample – collimator aperture (mm)	15.5 ± 1 (PP foils)
	20.5 ± 1 (Kapton foils)
Distance aperture – entrance window (mm)	10
Aperture opening diameter (mm)	3.6
Entrance window – Si chip (mm)	3
Thickness Si chip (μm)	500
Thickness Be window (μm)	8
Active area (mm <sup>2</sup> )	40
Tilt angle (degrees)	15.62

beam intensity was determined from a pre-calibrated diode. Since all spectra and diffraction data shown here were calibrated to the same intensity, the photon flux can be regarded constant at  $I_0 = 8.4 \times 10^9$  photons  $s^{-1}$ . At the same time of the diode measurement, a fluorescence spectrum was recorded and used to calibrate all other spectra to the amplitude of the Argon  $K_\alpha$  fluorescence line. The exposure time in the experiments was 1 s/pixel ( $> 40 \times 40$  points per neuron scan).

#### 2.4. X-ray fluorescence analysis

A tissue section was placed into the focus of the X-ray beam and was raster-scanned through the X-ray beam. At each scan point, XRF photons were recorded and spectrally analyzed. To quantify the amount of a given element within a cell, first the cell contour had to be defined. For this purpose, we used the signal distribution of Se, which matched the intracellular area of all cells very convincingly when comparing to optical micrography, where neurons were easily identified based on the presence of neuromelanin as a brown pigment. Using the Zn fluorescence signal for segmentation would be equally possible as in [18], but would not improve or change the analysis. Note that in [18] the primary beam energy was not sufficient to excite Se, so the choice was made for Zn. For every Se fluorescence map, the signal was first smoothed with a Gaussian filter and a threshold was chosen based on visual inspection such that two mutually exclusive areas, representative of the inside and outside of a cell, could be defined. In future threshold definition could easily be transferred to an unsupervised algorithm. The accuracy of discrimination was compared to optical micrographs of the same histological sections. If more than one cell was present within a scan, the intracellular area was defined for each cell separately. The spectra that were recorded in the respective areas were averaged using the nanodiffraction toolbox [20] available for MATLAB (Mathworks Inc.). The workflow of this procedure is visualized in Fig. 3.

For every individual cell the recorded XRF spectra were averaged to obtain one average spectrum per cell. In total, 53 cells were analyzed. Subsequently, the averaged spectra were imported into pyMCA [30] for energy calibration and fitting to extract spectral line intensities. In MATLAB all line intensities were rescaled to an exposure time of 1 s when necessary and transformed into absolute units of area density ( $g\ cm^{-2}$ ) using the NIST Standard Reference Material 1577b (bovine liver) as calibration standard. The averaged bovine liver spectrum shown in Fig. 4(A) was fitted using pyMCA and fit areas were rescaled to a reference exposure time  $t_{ref}$  of 1 s and an effective thickness  $d_{ref}$  of 30 μm to match the sample thickness.

Certified values for absolute concentrations in the bovine liver were used to obtain absolute concentrations within the human tissue. The absolute concentration  $c_i$  for a given element  $i$  was

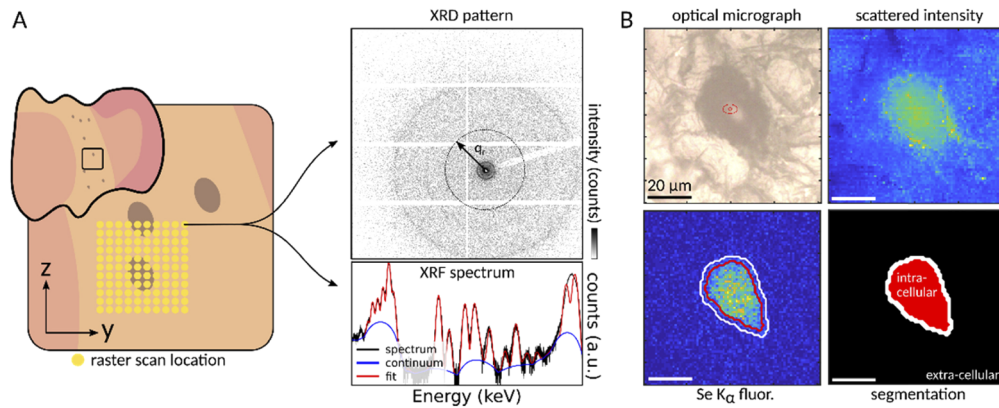


**Fig. 3.** Data collection and segmentation. (A) A tissue is raster scanned using a focused X-ray beam and a diffraction pattern and a fluorescence spectrum is recorded at each scan point. (B) Integrating the scattered intensity per image yields a darkfield image of the sample. In addition, the Se K $\alpha$  line from the XRF spectrum was integrated yielding a map of the Se K $\alpha$  fluorescence intensity. Se appears to be homogeneously distributed. Therefore, the Se fluorescence map was filtered with a Gaussian and a manual threshold was applied to each image to segment the image into two components: intra- and extracellular. The extracellular region was found by slightly enlarging and then inverting the intracellular area.

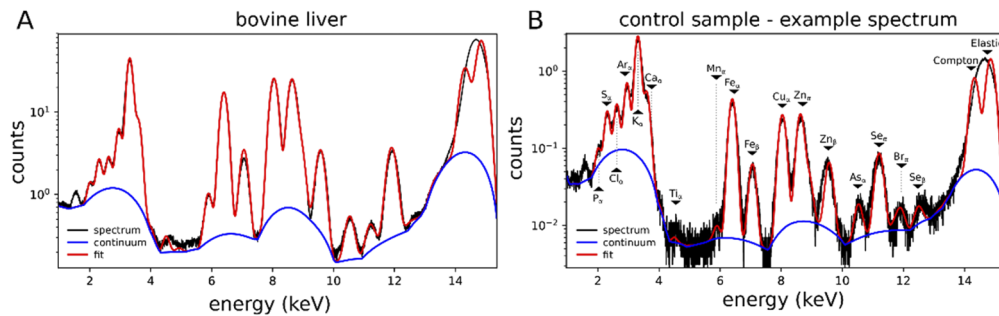


**Fig. 4.** Calibration of the XRF spectrum and an example spectrum from a control sample. (A) Average over 10000 individual spectra with 1 s counting time each from a 150  $\mu\text{m}$  thick bovine liver section. To avoid radiation damage, and to average out any eventual lateral variations, the spectra were recorded in form of a large scan. The model fit is indicated by a red line. The continuum background was identified using manually chosen parameters for the 'strip' filtering algorithm adopted by pyMCA. (B) Example average spectrum of an intracellular area of a control sample. In (A) and (B), the Compton and elastic scattering could not be resolved with the given instrumental setting. Note that minute amounts of titanium could be detected in both spectra, which is likely a contaminant in the collimation system of the fluorescence detector.

obtained from Eq. (1).

$$c_i = c_i^{\text{bov}} \cdot \left( \frac{A_{\text{Ar}}^{\text{bov}}}{A_{\text{Ar}}} \right) \cdot \left( \frac{A_i}{A_i^{\text{bov}}} \right) \cdot \left( \frac{d}{d_{\text{ref}}} \frac{t_{\text{ref}}}{t} \right) \quad (1)$$

where  $\left( \frac{A_{\text{Ar}}^{\text{bov}}}{A_{\text{Ar}}} \right)$  is the ratio of fit areas of the Argon K $\alpha$  line of the bovine liver and the sample,  $c_i^{\text{bov}}$  is the certified reference concentration of the element in the bovine liver and  $A_i^{\text{bov}}$  the fit area of the element in the bovine liver spectrum while  $A_i$  is the fit area of the element in the

sample spectrum.  $d$  is the thickness of the bovine liver, 150  $\mu\text{m}$ , and  $t$  is the exposure time. Bovine liver concentrations for a list of relevant elements are tabulated in Table 3. Note that identical mass densities of sample and calibrant tissue are assumed in Eq. (1). We believe this to be roughly justified for soft tissues when applying the same drying procedure. However, if the true mass densities would differ, which we cannot control, a corresponding systematic offset in concentration would result. Importantly, this would not affect the p-values of the statistical analysis, as the values for all cells measured would change by the same factor.

**Table 3. Relevant mass fractions and area densities for the NIST Standard Reference Material 1577b bovine liver. The area densities of the calibrant were used to determine the absolute concentrations in human brain tissue sections. X-ray emissions energies were obtained from [31]**

Element	$K_{\alpha 1}$ (keV)	mass fraction (g [100 g] $^{-1}$ )	area density (g cm $^{-2}$ )
K	3.31	0.994	$1.12 \times 10^{-8}$
Ca	3.69	160	$1.31 \times 10^{-12}$
Mn	5.90	10.5	$1.19 \times 10^{-13}$
Fe	6.40	184	$2.08 \times 10^{-12}$
Cu	8.05	160	$1.81 \times 10^{-12}$
Zn	8.64	127	$1.44 \times 10^{-12}$
As	10.54	0.05	$5.65 \times 10^{-16}$
Se	11.22	0.73	$8.25 \times 10^{-15}$
Br	11.92	9.7	$1.10 \times 10^{-13}$

The averaged bovine liver spectrum is shown in Fig. 4 together with a fitted spectrum from a control sample (intracellular area). Absolute elemental concentrations were calculated for all elements that could be detected in the sample. For the following analysis, concentrations for light elements (below 6 keV) should be regarded with caution, because the attenuation length  $\mu$  for hard X-rays scales with the photon energy  $E^{-3}$  and atomic number  $Z^4$  and hence fluorescence photons emitted from these lighter elements are more likely to be re-absorbed by the sample. We refrained from more elaborate corrections for self-absorption, described e.g. in [32–34], since the elements with lower photon energies are not of particular concern in this study, and since the statistical tests did not depend on the absolute concentration of each element.

### 2.5. Statistical analysis

Data were analyzed and displayed using python version 3.6.6. For display, the python modules matplotlib and seaborn were used. Normality tests were performed using the python package SciPy (version 1.0.0). The sufficient summary statistics approach has been implemented in Matlab (Mathworks, R2018b) based on analysis scripts provided in [35]. The nested ANOVA has been implemented in Matlab (R2018b) using the function anovan. A p-value greater than 0.05 was considered to indicate a statistically insignificant difference. The cluster analysis was performed using scikit-learn (version 0.20.1).

## 3. Results

### 3.1. Element quantification and mapping

We quantified concentrations of twelve trace elements inside and outside of 26 CO and 27 PD cells (see Data File 1). Five to seven cells were analyzed from four PD and four CO patients, respectively. Intra- and extracellularly, the following elements were detected: phosphorus, sulfur, chlorine, potassium, calcium, manganese, iron, copper, zinc, arsenic, selenium, and bromine. Intra- and extracellular element concentrations are reported in Fig. 5 except for low-Z elements

( $Z < 21$ ). In the following analyses we focus on the intracellular changes of trace element concentrations.

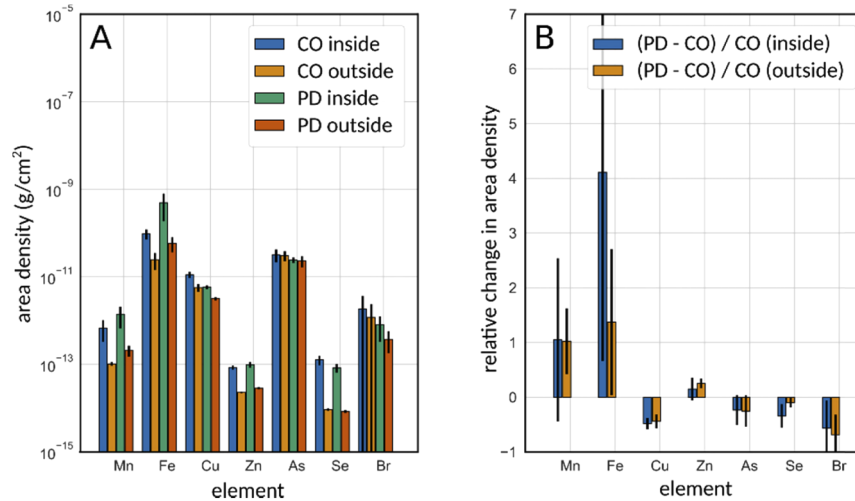


**Fig. 5.** Average absolute and relative trace element concentrations in midbrain neurons of the PD and CO group. (A) Absolute concentrations of trace elements inside and outside of neuromelanin-positive neurons of PD and control patients. Error bars indicate the standard error of the mean for all patients. (B) Relative changes in concentration of PD relative to the control. While a value of 1 corresponds to a 100% increase in concentration, a value of  $-0.5$  corresponds to a relative concentration of 50% of a specific element in the PD cohort in contrast to the control group.

In order to judge inter- and intra-group variances, it is instructive to inspect element concentrations per cell separately. Element data were visualized in a polar bar chart in Fig. 6. One can observe a strong cell-to-cell variability, although general trends such as higher Cu concentrations for cells from the CO group are observable. It is however possible to identify outliers, especially in case of Br where two cells from patient CO1 dominate the overall Br signal level.

Data shown in Fig. 6 can also be separated into categories, e.g. grouped by patients, as shown in Fig. 7. Upon categorization into patients, concentration levels can still fluctuate strongly due to a small cell number per patient, see for example Mn levels for PD3. Large variances are observed within one or two patients as in the distribution of Fe for patient PD3 in Fig. 7 or the distribution of Br in patient CO1 and PD1. Aggregating into the groups CO and PD produces similar distributions except for the case of Cu, Se and Br.

Before any statistical test, a parametric Shapiro-Wilk (SW) was performed to assess whether the data follow a normal distribution. Based on p-values from the SW test, nearly all distributions significantly deviate from a normal distribution (Table 4). Given this result, parametric testing such as t-testing is likely to be prone to errors. T-testing has the second disadvantage, that it can only be applied on the pooled data over all patients. If, however, a notable between-subject variation is present, the variance is usually underestimated leading to superficially small p-values. Two additional tests were therefore conducted that consider any between-subject variance. First, we used the sufficient summary statistics approach (SSS) [35]. The effect size was measured by the mean of a sample. We assumed random effects and inverse variance weighting to obtain a set of p-values listed in Table 4. In fact, the p-values are orders of magnitude larger than the values obtained from a classical t-test on pooled data. In the second test, data was analyzed with a nested ANOVA (nANOVA) while assuming random effects. As for the SSS, data was modelled as two-layer dataset with the first layer being the disease type (PD or CO), while the second

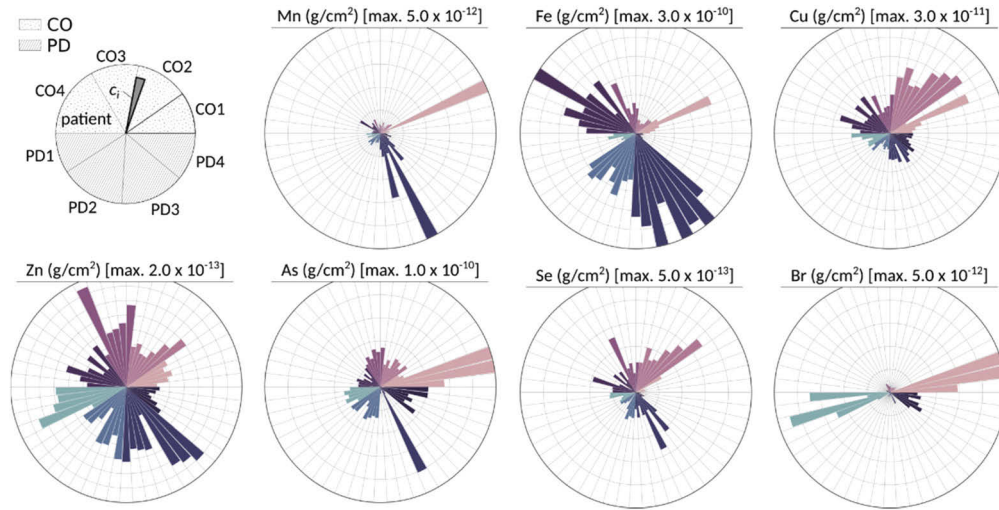


**Fig. 6.** Polar bar diagram of elemental concentrations in SN neurons. Each bar corresponds to a single cell. The upper half of each polar plot corresponds to data from a control group. Shades within each group indicate the individual patient.

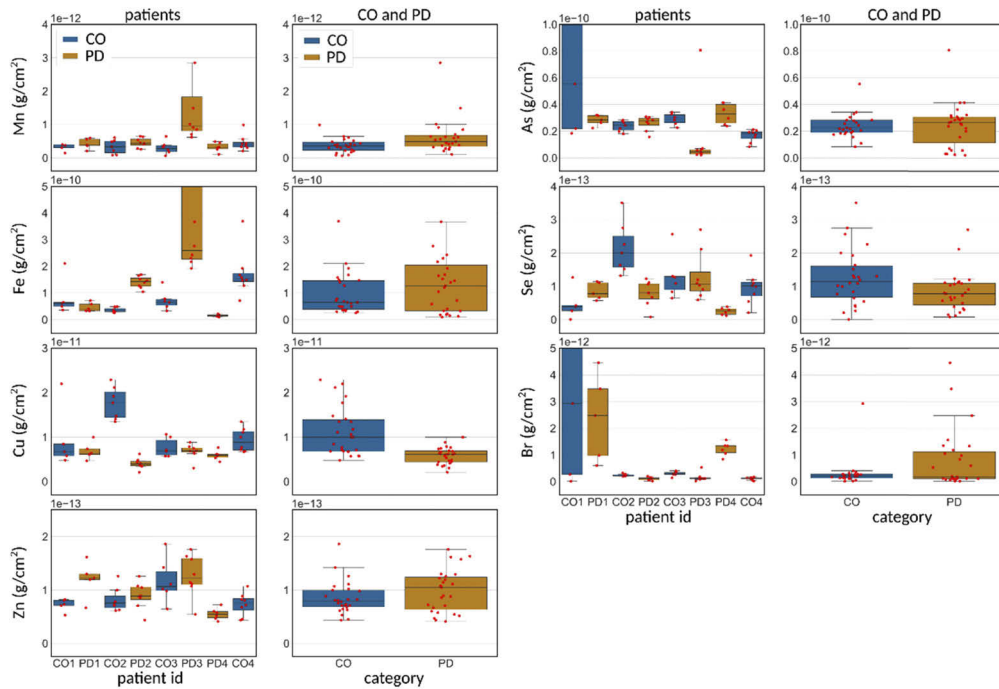


**Fig. 7.** Box-Whisker plot for two different groupings of the dataset. Cell concentrations grouped by patients and categories CO and PD (color coded). Interindividual variations can increase the variance in the distributions for the CO and PD groupings, as e.g. seen in the CO group for Cu (third row).

layer comprising individual patients (PD1 through PD4 and CO1 through CO4). The smallest values for the SSS and nANOVA approach, although slightly above the arbitrary 5%  $\alpha$ -level (in both cases 0.07 for Cu), are highlighted in bold in Table 4 to indicate that Cu is the most discriminatory element in this dataset. Both analyses also show that inter-individual variation needs to be carefully considered and that, both, a larger set of patients and more recordings of intracellular concentrations should be used.

**Table 4. List of p-values. To take into account interindividual variation, the sufficient-summary-statistic approach (SSS) described in [35] as well as a nested ANOVA (nANOVA) was used. In both approaches, random effects were assumed. In the second and third row, where the results of the Shapiro-Wilk test (SW) are reported for the CO and PD group, p-values larger than the 5% are printed in bold, indicating that the observed distribution is no rare statistical realization under the assumption of a normal distribution as the null hypothesis. In the fourth and fifth row, the SSS and nANOVA results are tabulated with the smallest p-values highlighted.**

Element	SW (CO)	SW (PD)	SSS	nANOVA
Mn	4.04e-10	1.71e-10	1.00	0.64
Fe	1.14e-4	1.32e-10	0.82	0.42
Cu	6.20e-3	<b>9.79e-1</b>	<b>0.07</b>	<b>0.07</b>
Zn	5.79e-3	<b>2.00e-1</b>	0.51	0.57
As	9.94e-8	1.65e-3	0.96	0.45
Se	<b>1.67e-1</b>	3.09e-3	0.26	0.34
Br	3.53e-10	4.71e-6	0.36	0.52

Since the variability in the ion concentration seems too large for a significant discrimination between classes, we investigated whether this limitation could be lifted by an unsupervised classification scheme based on the complete seven-dimensional dataset (Mn, Fe, Cu, Zn, As, Se, Br).

Each data point was classified using k-means clustering to compare with its *a priori* known class (PD or CO). The result is shown in Fig. 8, where data for five relevant elements (Fe, Cu, Zn, As and Se) were visualized. Already by inspection of for example columns two to four in the second row, one can gain the impression of higher Cu levels in the CO group, in line with the results of the statistical tests. However, no clear separation ‘by eye’ into classes is evident. The k-means algorithm was run for  $k=2$  such that the algorithm returns only two labels that could in turn be compared to the label CO or PD. To improve the robustness of the classification, outliers, having a concentration lower or higher than the interquartile range of the distribution for all cells, were removed prior to classification. It is found that the clustering algorithm associated the correct label in 65.6% of the cases. Although our data show group differences in elemental concentrations, high variances within groups disallow automated group classification resulting in a negligible prediction rate.

### 3.2. Lewy body characterization

Because  $\alpha$ -synuclein-containing LBs represent a hallmark of PD and  $\alpha$ -synuclein aggregation can be fostered by various transition metals, the elemental content in LBs was analyzed using spatially resolved XRF maps, while any crystalline or paracrystalline material should give rise to a characteristic diffraction signal. To identify LBs, Kapton foil was used as sample support because it enables histochemical staining while still allowing for later use as sample window. Following the identification of a LB from histology (Fig. 9(D)), the area of the LB was scanned for element quantification and diffraction analysis. Since LBs are sparsely distributed and scan times and x-ray alignment were also time-consuming, we were only able to scan two LBs in this study. Although an  $n=2$  is not sufficient to obtain statistically relevant results, we included this

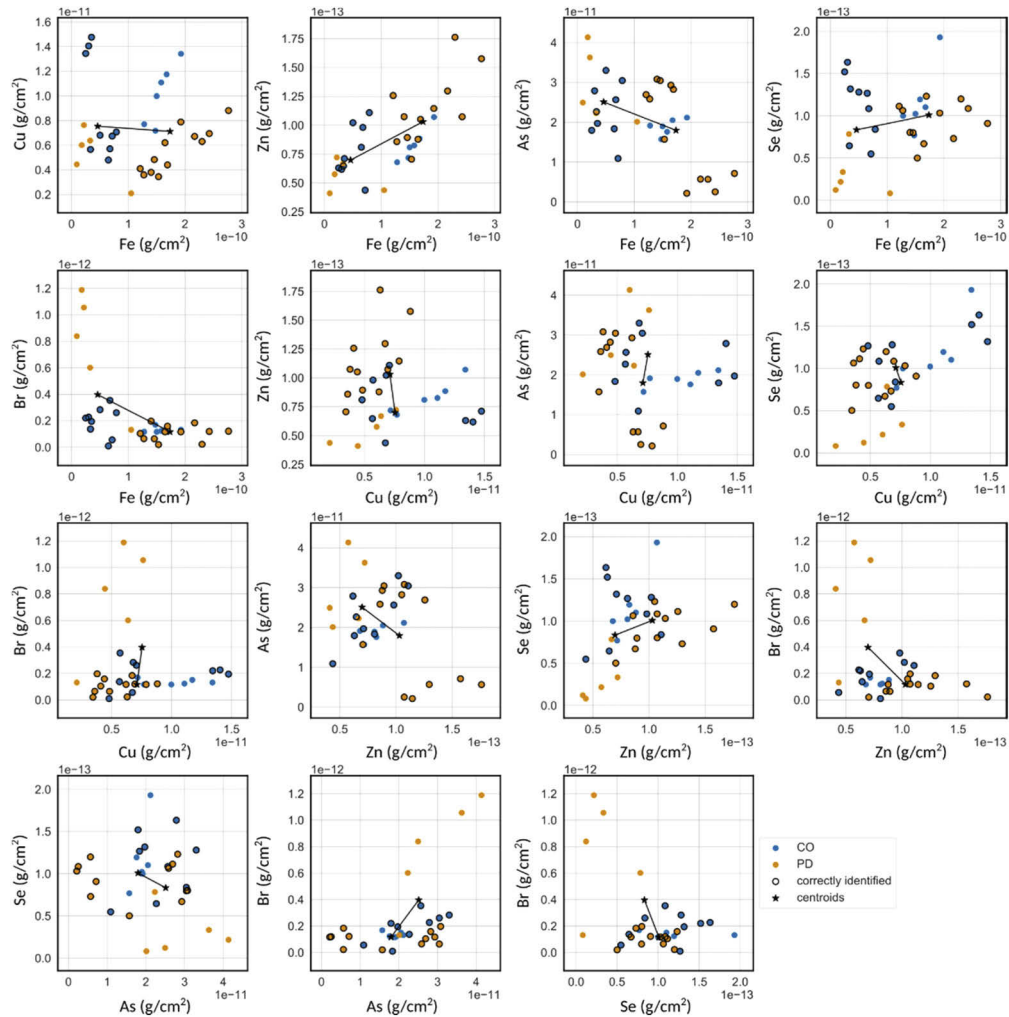


**Fig. 8.** Two-dimensional representation of the k-means clustering. The clustering algorithm was applied on seven spectral lines. Prior to the analysis, outliers (defined as having a concentration lower or higher than the interquartile range of the distribution for all cells) were removed from the dataset. The k-means algorithm was run for  $k = 2$  such that the algorithm returns two labels. Each label was then assigned to the class CO and PD, respectively. Matching classes were outlined with a solid black line. The two centroids were marked with black stars and the distance between the centroids was indicated by a black solid line. Overall, 65.6% of all datapoints were correctly identified.

analysis as a contribution to method development, demonstrating that the signal and contrast levels are compatible with our other XRD and XRF analyses.

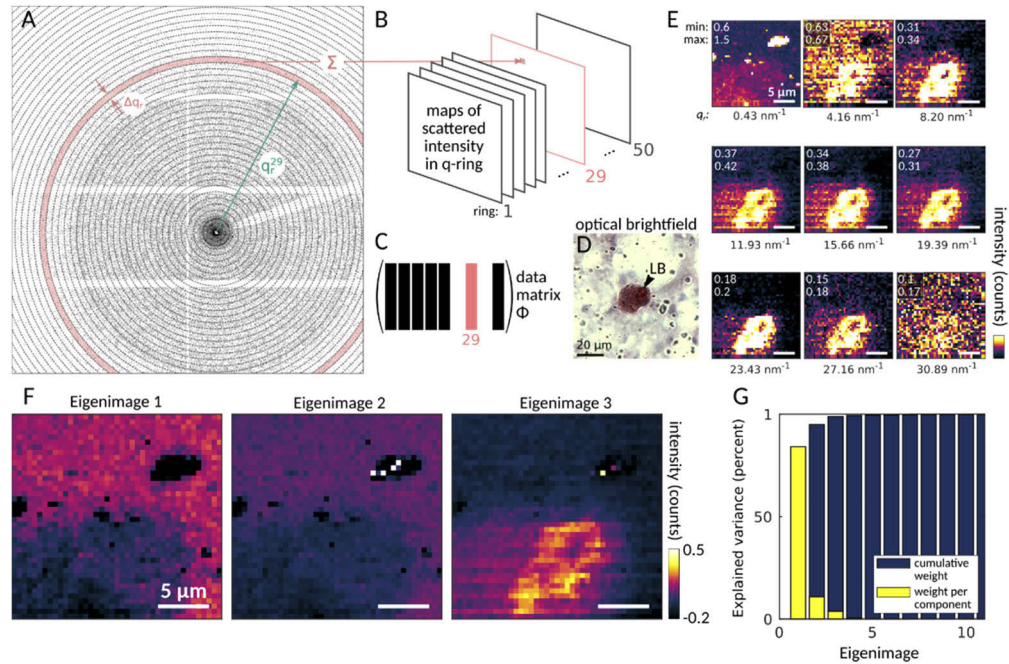


**Fig. 9.** Eigenimage analysis using principal component decomposition and reconstruction. (A-C) Data processing pipeline. (A) Each diffraction pattern is split into a fixed number of rings (here, 50) with a fixed  $q$ -interval of  $0.86 \text{ nm}^{-1}$ . (B) A darkfield image is calculated for each ring separately. Each image is then added as a column vector into the data matrix  $\Phi$  shown in (C) for decomposition. (D) Optical brightfield image of a LB visualized by new fuchsin staining and indicated by a black arrow. (E) Nine exemplary darkfield maps of a raster scan covering a LB. The central  $q$  value is noted underneath of each image. Intensity limits are indicated above each frame. The covariance matrix of the data matrix  $\Phi$  was diagonalized using principal component analysis. The three largest components (eigenimages) are depicted in (F). The weight of each component is shown in (G).

The diffraction data were analyzed by calculating 50 diffraction maps from a single scan, where each map was obtained by integrating the diffraction pattern within a small  $q$ -interval, as sketched in Fig. 9(A)-(B). As an example, nine diffraction maps are shown in Fig. 9(E). Based on the resulting set of 50 diffraction maps, a principal component analysis was performed to obtain the eigenimages (or, eigen-diffraction maps). This was accomplished by transforming each image into a column vector and collecting all vectors in a data matrix  $\Phi$ , as shown in Fig. 9(C). The data matrix was transformed into a covariance matrix for diagonalization as described in [21]. The eigenvectors were then transformed into their two-dimensional representation. The three principal components are shown in Fig. 9(F). As shown in Fig. 9(G), the first three eigenimages account for almost 99% variation in the dataset.

The original darkfield maps can be approximately reconstructed from a linear combination of the first three eigenimages. The weights for each component were determined by least-squares minimization of the difference between the composed and the original image. The distribution of weights as a function of the scattering vector is shown in Fig. 10(A). The scattering vector is defined as  $q = (4\pi/\lambda) \sin(\theta)$ , where  $\lambda$  is the wavelength of the radiation and  $2\theta$  the scattering angle between the primary and scattered beam. Black arrows mark the position of the darkfield

maps shown in Fig. 9(E). We highlight that the third eigenimage accounts for a feature that is indicative of a LB and whose composition is quantified by XRF. The scattering distribution of the feature covers a broad range of  $q$ -values, with a peak at  $13.6 \text{ nm}^{-1}$ . A similar distribution can be obtained in a less automated way by thresholding eigenimage 3 such that only scattering data from within the LB is averaged and similarly for a manually chosen background region. The averaged background signal is subtracted from the scattering data obtained from the LB and the signal is azimuthally integrated to obtain the curve shown in Fig. 10(B). Once again, the same shape of the distribution as for eigenimage 3 is obtained with a prominent peak at  $13.6 \text{ nm}^{-1}$ , which is the scattering peak of dried  $\alpha$ -synuclein pellets. This scattering signal, however, is quite generic for protein secondary structure, in particular for  $\beta$ -sheets, so that the conclusion that  $\alpha$ -synuclein crystals cause the WAXS scattering cannot be drawn. In fact, scattering distributions from cells of control patients obey the same general shape of the diffraction curve (Fig. 10(B)).

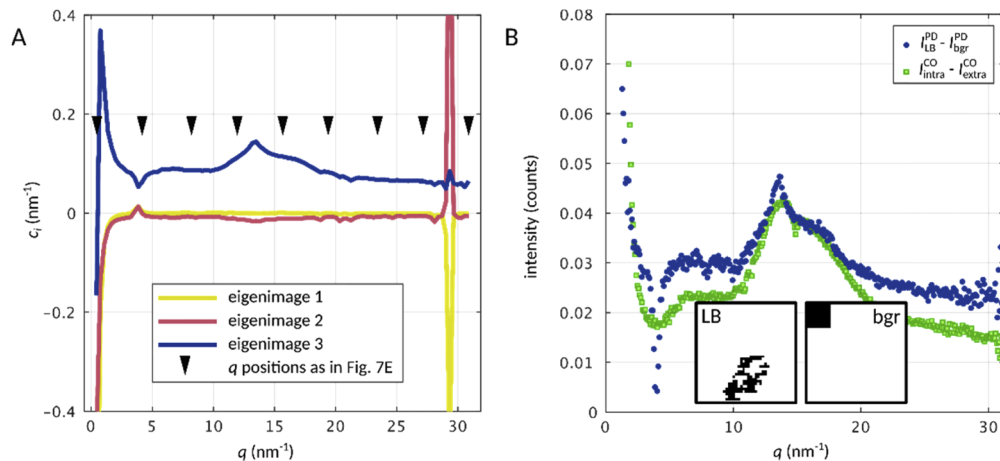


**Fig. 10.** Distribution of the scattering signal from the LB along  $q$ . Since each darkfield map can be approximated by a weighted sum of the three eigenimages corresponding to almost 99% variation in the dataset, the distribution of these components along  $q$  is shown in (A). Positions of the darkfield maps shown in Fig. 9(E) are marked with black arrows. The eigenimage representing the LB (eigenimage 3) was thresholded and the scattering data from all scan points with a total scattering intensity greater than the specified threshold was averaged and azimuthally averaged. Similarly, a background region was manually chosen and the scattering data was averaged, azimuthally integrated and subtracted from the LB scattering. The background-subtracted one-dimensional intensity is shown in (B), clearly representing the  $q$ -distribution for eigenimage 3. The distribution is similar to the  $q$ -distribution of scattering from a cell by a control patient (CO1).

To shed light onto the chemical composition of LBs, the fluorescence signal was analyzed. The region of the first measured LB (previously described in Fig. 9) highly overlaps with the fluorescence maps of Br, As and Se, as shown in Fig. 11(A,C). Fe is distributed within and around the LB in the measured cell. In contrast the fluorescence signal within this LB anti-correlates with the distribution of Cu. Small features appearing at low  $q$  are primarily composed of low-Z elements such as K and Ca. A second LB originating from another PD patient was scanned in the same fashion, see Fig. 11(D). Again, Br fluorescence is highly localized. Fe is again distributed within the measured cell including the LB region and Cu anti-correlates with the region of the LB.

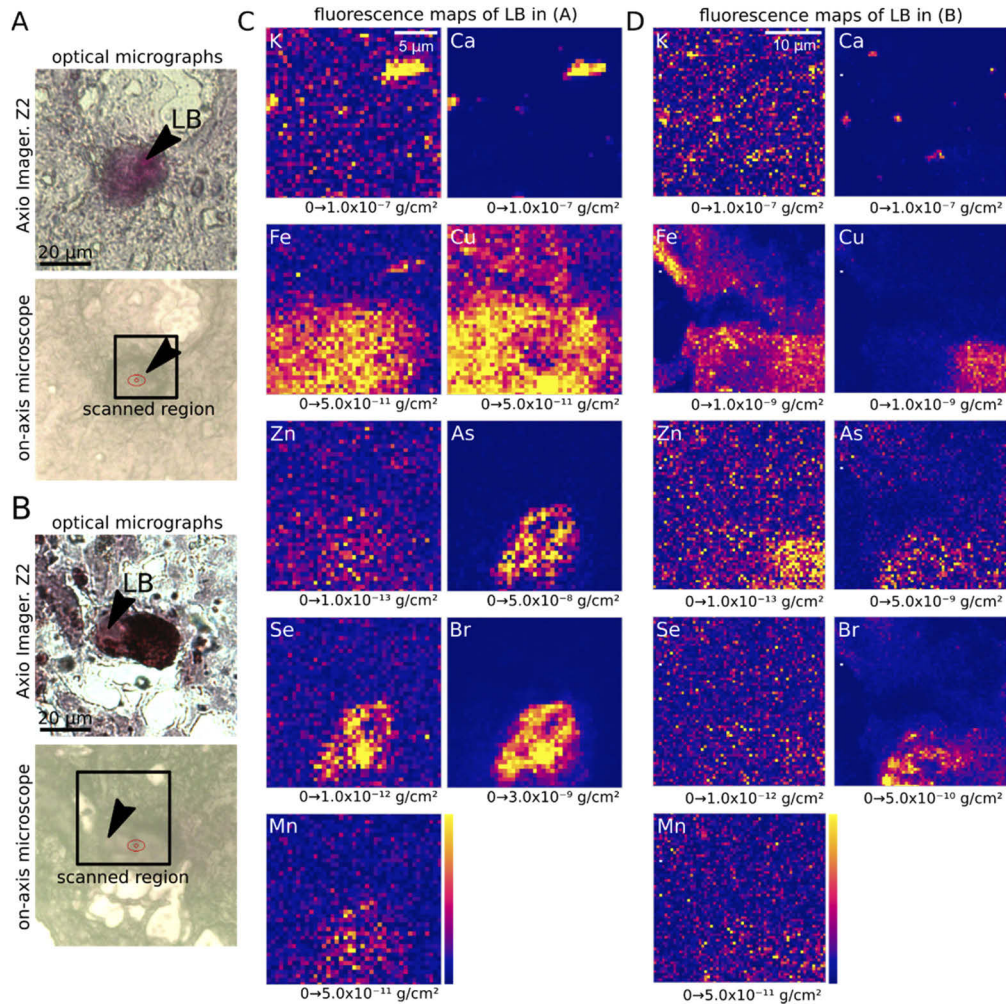


**Fig. 11.** XRF analysis of a raster scan covering two LBs. (A,B) Optical brightfield images of two histological sections containing LBs. The location of each LB is marked by a black arrow. The scanned region is approximately marked by a black frame. An optical micrograph as seen after the sample was mounted onto the motorized stage of the X-ray setup is shown underneath each image indicating the LB. (C) XRF maps of a LB shown in (A). Ranges of the color scale are given below each sub-figure. K and Ca are dominant components of a feature that is also shown in eigenimage 2 in Fig. 9. Fe is homogeneously distributed within the cell while Cu concentrations are reduced in the vicinity of the LB. The presence of a LB co-localizes with As, Se and Br and, in part, Mn. In (D), Br and As are co-localized in the LB.

#### 4. Discussion

Iron dyshomeostasis and accumulation inside the SN is widely observed in MRI studies with PD patients. Therefore, nigral Fe load is discussed to be a biomarker for the disease [36]. However, biomarker approaches analyzing serum, plasma or CSF samples indicate that not only Fe but also other trace elements are dysregulated in the disease-state, assuming a specific elemental profile of PD [23,24,26,27]. So far, a convincing quantification of trace elements inside nigral neurons is missing and their distribution in LBs has not been described. In this study, we analyzed postmortem midbrain tissue from PD patients and controls by using XRD to localize and characterize crystalline structures and XRF to quantify elemental concentrations in neuromelanin-pigmented neurons and LBs. Regarding the analysis of XRD data, we introduced a model-independent approach of principal component analysis.

The fluorescence analysis points to moderately different amounts of trace elements such as Fe and Cu in PD tissue compared to the age-matched control with a high intra- and interindividual variance. A dyshomeostasis of respective trace elements has been reported in previous X-ray based analyses [37,38]. One of these studies using synchrotron radiation detected significant differences in S, Cl, Fe, Ca and Zn in nigral neurons of PD compared to control patients, whereas differences of P, S, Cl, Rb, Fe and Zn were significant in the extracellular space. However, they already showed strong variances in the element concentrations [38].

Our study could not show a significant Fe increase in PD, so that our data cannot confirm a global Fe enrichment in SN neurons of PD patients. In general, we observed strong interindividual and intraindividual differences for all measured elements, especially Fe, which prevented us from identifying any statistically significant difference between the groups. These observations are not in line with a previous investigation analyzing nigral neuromelanin-positive cells of patients and controls which could show increased Fe levels for PD patients by using a laser microprobe mass analyser [39]. These results were confirmed by studies using particle-induced X-ray emission (PIXE) or XRF. Surprisingly, it does not seem to make a difference if iron content is measured within single neuromelanin-positive neurons analyzed by PIXE and XRF [37] or within a whole SN section using rapid-scanning XRF mapping [40]. In both cases a significant Fe increase was observed for PD patients compared to controls. In our study, the local XRF analysis of single neurons likely induced high variance in our output, since elemental concentrations were not averaged over extensive SN areas. The results suggest using a larger beam and larger step sizes in further experiments to increase the sample size and the measured area. In addition, it was not possible to further characterize the scanned SN area, e.g. regarding different nigrosomes. Our findings have direct clinical implications as they demonstrate that there is a high heterogeneity in the nigral Fe content in PD patients. Because currently the concept of conservative iron chelation is evaluated as novel disease-modifying treatment option for PD (NCT02655315), it is important to understand that increased iron concentrations may be present only in a subgroup of patients, which may affect the clinical response.

On the other hand, we found a marginal significant reduction in Cu levels in the PD samples, which confirms the previously reported Cu dyshomeostasis in PD (e.g. [3]). In PIXE and XRF, reduced Cu levels have been reported in nigral neurons of PD and LBD patients [37]. In addition to the known PD-related elements Fe and Cu, Se appears to be an interesting dysregulated trace element in PD. Se has been reported to be significantly increased in plasma levels of PD patients [27], which was confirmed in CSF levels [26]. Interestingly, epidemiological analysis of soil composition showed that geographical regions with high Se concentration show a lower rate of PD mortality, highlighting the potential relevance of Se for PD [41]. Here we observed no significant difference in the Se amounts within dopaminergic neurons of PD and CO samples.

Similar to the already mentioned Fe, Cu and Se concentrations, amounts of As, Zn and Mn showed a strong intercellular variation in our study. Data on Mn and Zn confirm results of a ICP-MS study analyzing SN tissue of PD and control samples [12]. Another study showed

that Zn content is often reduced in brain regions where iron is increased, as within the SN, and vice versa [40]. However, regarding the Zn content within neuromelanin-positive neurons, no significant difference was found between PD and control group using PIXE [37]. The origin of high Br levels in some cells still lacks a suitable explanation, as it is unlikely to stem from sample contamination. Br has been detected in SN neurons in another PD study also showing high interindividual variances for Br [38]. These findings may give rise to the speculation that some patients were taking occasionally bromine-containing medication such as the anti-anxiety agent bromazepam or bromocriptine, an ergoline dopamine agonist that was previously widely used for the treatment of PD. However, medical records of our patients did not document the use of these drugs.

Furthermore, we analyzed the intracellular seven-dimensional dataset to search for specific clusters, representing PD and control patients. Based on the concentrations of Fe, Zn, Cu, Se, As, Mn and Br, unsupervised clustering reached a discrimination rate of 65.6%. While this discrimination rate is unsatisfactory in terms of classification, cluster analysis can still be interpreted to identify the relevant elements for separation (multiple discrimination analysis). In [38], Cl, Fe, Br, Ca and Zn were shown to be significant elements for clustering into PD and control group based on the SN neuron concentrations. A recent CSF-based study revealed an elemental cluster including Se, Fe, As, Ni, Mg and Sr, which discriminated PD from control samples using machine-learning algorithms [26]. It seems likely, that the elemental profile of PD depends on the biological source material (e.g. brain tissue, CSF, serum, plasma).

Previous studies showed that the detection method may also influence the detected output. For example, PIXE and EDX were used for general analysis of the elemental content of SN tissue from patients without neuropathological findings. With PIXE Fe, Mn, Cr and Zn were detected, whereas EDX was able to quantify Fe, Zn, Al and Si within the tissue [42]. Different methods of generating XRF should be combined and compared to complete the element profile of PD.

Another general dilemma on studying tissue from PD patients of high age is the heterogeneity regarding the medical records of age-matched controls. In our study, three control patients were suffering from different kinds of cancer and one patient from MS. Including these different disease types to the control group can induce a stronger heterogeneity of the control data. Possibly these patients do not completely reflect the elemental profile of the population not suffering from PD. On the other hand, brain samples of patients without clear pathology and an extensive medical record are sparse in brain bank material, and any study with human tissue must consider these limitations. Aiming to reveal statistically significant differences in trace element concentrations comparing PD patients and controls, further studies are encouraged to use a larger field of view and higher sample throughput.

Since LB pathology, as a PD characteristic, cannot be fully simulated *in vitro* or *in vivo*, methods with high spatial resolution are required to investigate these subcellular protein inclusions in human tissue. Explicitly, the question arose if  $\alpha$ -synuclein can be detected without any processing of the tissue. In general, XRD is capable to non-invasively detect crystalline arrangements in tissue at high spatial resolution. In this study, XRD data remained inconclusive to whether or not  $\alpha$ -synuclein is present in the LB, while it may be taken as an indication that higher amounts of  $\beta$ -sheet proteins are present, compared to neurons of control patients.

Regarding the elemental content of LBs, little is known so far. Up to now, LBs were analyzed by immunohistochemical stainings showing Fe deposits overlapping with LBs [7]. However, it is unknown whether also other elements are enriched and how they are distributed inside LBs. Since studies suggested that elements such as Fe, Cu or Mn could foster  $\alpha$ -synuclein aggregation [8], an enrichment of these elements in LBs containing  $\alpha$ -synuclein aggregates was conceivable. Although Fe is known to bind  $\alpha$ -synuclein [43,44], *in vitro* studies showed that Fe could also induce  $\alpha$ -synuclein aggregation indirectly [45–47], hypothesizing that Fe does not mandatorily cluster with  $\alpha$ -synuclein aggregates in LBs. A LA-ICP-MS study analyzing the elemental content

of  $\alpha$ -synuclein aggregates in the olfactory bulb of PD patients showed a decrease in Fe and Cu level [48]. In the current study, we investigated which trace elements can be detected in LBs of PD affected tissue using sub-micron focusing. The signal level allowed for the analysis of nine elements. A pronounced Br signal in the LB was unexpected and could be possibly explained by Naphthol AS-BI phosphate addition during the staining procedure. Overall, we observe a heterogeneous trace elemental composition comparing two analyzed LBs, and it is clear that the sample size must be increased, which requires a more efficient correlative microscopy approach and probably also relaxed resolution to cover larger areas, see below.

## 5. Conclusion

The present study shows that high resolution scanning XRF and XRD are sensitive techniques for tissue investigation on the single cell level, which allows for quantitative characterization of neuromelanin-positive neurons in PD samples. We describe the intracellular presence of Fe, Cu, Zn, Mn, As, Se and Br in PD and control patients. As a result, we detect large inter- and intraindividual variances in trace element concentrations. This surprising heterogeneity puts in question the existence of a clearly defined and general dyshomeostasis in PD. For example, Fe concentration differences between PD and control samples as assumed by our previous study [18] using one patient per group could not be confirmed by the present analysis of a larger sample size. The heterogeneity could eventually be explained by the presence of pathological subtypes in PD. In fact, not only the large variance of PD but also of the age-matched control samples presents an interesting finding in itself, which should be further studied in view of trace metal regulation and environmental factors.

By increasing the spatial resolution with respect to a previous analysis, we demonstrate the versatility of an X-ray-based microanalysis. We also show that elemental profiling by XRF and diffraction-based LB characterization can be combined with subcellular resolution in real space. Presenting an innovative unsupervised eigenimage (PCA) approach to identify LBs based on the scattering signal, the current study provides a useful tool for future XRD-based LB characterization. Overall, the present study shows that hard X-ray microscopy of tissues is a promising technique to further research on PD. However, an important recommendation for future extension of this work is to combine different resolution by variation of the focal spot size. Much larger field of views need to be scanned with a tenfold larger beam in order to probe more neurons per tissue section, and also sections from many more individuals. At the same time, after scaling up the throughput, the ability to zoom into certain regions of interest to be scanned with sub- $\mu\text{m}$  spot size will maintain sub-cellular resolution where needed.

## Funding

Deutsche Forschungsgemeinschaft (EXC 171, EXS 2067, SFB 937).

## Acknowledgements

We would like to thank Elisabeth Barski for assistance during sample preparation and Lucas Caldi Gomes for helping to assemble and seal the Kapton and polypropylene rings. Assistance during beamtime by Manfred Burghammer is gratefully acknowledged. We thank Julie Villanova for proving the bovine liver calibration standard. Tissue samples and associated clinical and neuropathological data were supplied by the Parkinson's UK Brain Bank, funded by Parkinson's UK, a charity registered in England and Wales (258197) and in Scotland (SC037554). We acknowledge support by the Open Access Publication Funds of the Göttingen University and by the DFG Cluster of Excellence Nanoscale Microscopy and Molecular Physiology of the Brain (CNMPB), Göttingen.

## Disclosures

The authors declare that there are no conflicts of interest related to this article.

## References

1. R. B. Postuma, D. Berg, M. Stern, W. Poewe, C. W. Olanow, W. Oertel, J. Obeso, K. Marek, I. Litvan, A. E. Lang, G. Halliday, C. G. Goetz, T. Gasser, B. Dubois, P. Chan, B. R. Bloem, C. H. Adler, and G. Deuschl, "MDS clinical diagnostic criteria for Parkinson's disease," *Mov. Disord.* **30**(12), 1591–1601 (2015).
2. D. Berg, K. Marek, G. W. Ross, and W. Poewe, "Defining at-risk populations for Parkinson's disease: Lessons from ongoing studies," *Mov. Disord.* **27**(5), 656–665 (2012).
3. D. T. Dexter, A. Carayon, F. Javoy-Agid, Y. Agid, F. R. Wells, S. E. Daniel, A. J. Lees, P. Jenner, and C. D. Marsden, "Alterations in the Levels of Iron, Ferritin and Other Trace Metals in Parkinson's Disease and Other Neurodegenerative Diseases Affecting the Basal Ganglia," *Brain* **114**(4), 1953–1975 (1991).
4. D. Devos, C. Moreau, J. C. Devedjian, J. Kluza, M. Petruault, C. Laloux, A. Jonneaux, G. Ryckewaert, G. Garçon, N. Rouaix, A. Duhamel, P. Jissendi, K. Dujardin, F. Auger, L. Ravasi, L. Hopes, G. Grolez, W. Firdaus, B. Sablonnière, I. Strubi-Vuillaume, N. Zahr, A. Destée, J.-C. Corvol, D. Pörtl, M. Leist, C. Rose, L. Defebvre, P. Marchetti, Z. I. Cabantchik, and R. Bordet, "Targeting Chelatable Iron as a Therapeutic Modality in Parkinson's Disease," *Antioxid. Redox Signaling* **21**(2), 195–210 (2014).
5. A. Martin-Bastida, R. J. Ward, R. Newbould, P. Piccini, D. Sharp, C. Kabba, M. C. Patel, M. Spino, J. Connelly, F. Tricta, R. R. Crichton, and D. T. Dexter, "Brain iron chelation by deferiprone in a phase 2 randomised double-blinded placebo controlled clinical trial in Parkinson's disease," *Sci. Rep.* **7**(1), 1398 (2017).
6. B. Fernández, I. Ferrer, F. Gil, and S. Hilfiker, "Biomonitorization of iron accumulation in the substantia nigra from Lewy body disease patients," *Toxicol. Rep.* **4**, 188–193 (2017).
7. R. J. Castellani, S. L. Siedlak, G. Perry, and M. A. Smith, "Sequestration of iron by Lewy bodies in Parkinson's disease," *Acta Neuropathol.* **100**(2), 111–114 (2000).
8. E. Carboni and P. Lingor, "Insights on the interaction of alpha-synuclein and metals in the pathophysiology of Parkinson's disease," *Metallomics* **7**(3), 395–404 (2015).
9. K. Joppe, A.-E. Roser, F. Maass, and P. Lingor, "The Contribution of Iron to Protein Aggregation Disorders in the Central Nervous System," *Front. Neurosci.* **13**, 15 (2019).
10. V. N. Uversky, J. Li, and A. L. Fink, "Metal-triggered structural transformations, aggregation, and fibrillation of human  $\alpha$ -synuclein: A possible molecular link between parkinson's disease and heavy metal exposure," *J. Biol. Chem.* **276**(47), 44284–44296 (2001).
11. A. Biesemeier, O. Eibl, S. Eswara, J. N. Audinot, T. Wirtz, G. Pezzoli, F. A. Zucca, L. Zecca, and U. Schraermeyer, "Elemental mapping of Neuromelanin organelles of human Substantia Nigra: correlative ultrastructural and chemical analysis by analytical transmission electron microscopy and nano-secondary ion mass spectrometry," *J. Neurochem.* **138**(2), 339–353 (2016).
12. S. Genoud, B. R. Roberts, A. P. Gunn, G. M. Halliday, S. J. G. Lewis, H. J. Ball, D. J. Hare, and K. L. Double, "Subcellular compartmentalisation of copper, iron, manganese, and zinc in the Parkinson's disease brain," *Metallomics* **9**(10), 1447–1455 (2017).
13. C. J. Fahrni, "Biological applications of X-ray fluorescence microscopy: exploring the subcellular topography and speciation of transition metals," *Curr. Opin. Chem. Biol.* **11**(2), 121–127 (2007).
14. T. Salditt and T. Dučić, "X-Ray Microscopy for Neuroscience: Novel Opportunities by Coherent Optics," in *Super-Resolution Microscopy Techniques in the Neurosciences*, E. F. Fornasiero and S. O. Rizzoli, eds. (Humana Press, 2014), pp. 257–290.
15. S. Vogt, J. Maser, and C. Jacobsen, "Data analysis for X-ray fluorescence imaging," *J. Phys.* **IV** **104**, 617–622 (2003).
16. S. C. Dodani, D. W. Domaille, C. I. Nam, E. W. Miller, L. A. Finney, S. Vogt, and C. J. Chang, "Calcium-dependent copper redistributions in neuronal cells revealed by a fluorescent copper sensor and X-ray fluorescence microscopy," *Proc. Natl. Acad. Sci.* **108**(15), 5980–5985 (2011).
17. M. W. Bourassa and L. M. Miller, "Metal imaging in neurodegenerative diseases," *Metallomics* **4**(8), 721–738 (2012).
18. E. Carboni, J.-D. Nicolas, M. Töpferwien, C. Stadelmann-Nessler, P. Lingor, and T. Salditt, "Imaging of neuronal tissues by x-ray diffraction and x-ray fluorescence microscopy: evaluation of contrast and biomarkers for neurodegenerative diseases," *Biomed. Opt. Express* **8**(10), 4331 (2017).
19. J. F. Collingwood and F. Adams, "Chemical imaging analysis of the brain with X-ray methods," *Spectrochim. Acta, Part B* **130**, 101–118 (2017).
20. J.-D. Nicolas, M. Bernhardt, A. Markus, F. Alves, M. Burghammer, and T. Salditt, "Scanning X-ray diffraction on cardiac tissue: automatized data analysis and processing," *J. Synchrotron Radiat.* **24**(6), 1163–1172 (2017).
21. M. Bernhardt, M. Priebe, M. Osterhoff, C. Wollnik, A. Diaz, T. Salditt, and F. Rehfeldt, "X-Ray Micro- and Nanodiffraction Imaging on Human Mesenchymal Stem Cells and Differentiated Cells," *Biophys. J.* **110**(3), 680–690 (2016).
22. D. T. Dexter, F. R. Wells, A. J. Lee, F. Agid, Y. Agid, P. Jenner, and C. D. Marsden, "Increased Nigral Iron Content and Alterations in Other Metal Ions Occurring in Brain in Parkinson's Disease," *J. Neurochem.* **52**(6), 1830–1836 (1989).

23. S. S. S. J. Ahmed and W. Santosh, "Metalloomic profiling and linkage map analysis of early parkinson's disease: A new insight to aluminum marker for the possible diagnosis," *PLoS One* **5**(6), e11252 (2010).
24. M. K. Gangania, J. Batra, S. Kushwaha, and R. Agarwal, "Role of Iron and Copper in the Pathogenesis of Parkinson's Disease," *Indian J. Clin. Biochem.* **32**(3), 353–356 (2017).
25. M. L. Hegde, P. Shanmugavelu, B. Vengamma, T. S. S. Rao, R. B. Menon, R. V. Rao, and K. S. J. Rao, "Serum trace element levels and the complexity of inter-element relations in patients with Parkinson's disease," *J. Trace Elem. Med. Biol.* **18**(2), 163–171 (2004).
26. F. Maass, B. Michalke, A. Leha, M. Boerger, I. Zerr, J.-C. Koch, L. Tönges, M. Bähr, and P. Lingor, "Elemental fingerprint as a cerebrospinal fluid biomarker for the diagnosis of Parkinson's disease," *J. Neurochem.* **145**(4), 342–351 (2018).
27. H.-W. W. Zhao, J. Lin, X.-B. B. Wang, X. Cheng, J.-Y. Y. Wang, B.-L. L. Hu, Y. Zhang, X. Zhang, and J.-H. H. Zhu, "Assessing Plasma Levels of Selenium, Copper, Iron and Zinc in Patients of Parkinson's Disease," *PLoS One* **8**(12), e83060 (2013).
28. K. Araki, N. Yagi, Y. Ikemoto, H. Yagi, C. J. Choong, H. Hayakawa, G. Beck, H. Sumi, H. Fujimura, T. Moriwaki, Y. Nagai, Y. Goto, and H. Mochizuki, "Synchrotron FTIR micro-spectroscopy for structural analysis of Lewy bodies in the brain of Parkinson's disease patients," *Sci. Rep.* **5**(1), 17625 (2015).
29. G. Ashiotis, A. Deschildre, Z. Nawaz, J. P. Wright, D. Karkoulis, F. E. Picca, and J. Kieffer, "The fast azimuthal integration Python library: pyFAI," *J. Appl. Crystallogr.* **48**(2), 510–519 (2015).
30. V. A. A. Solé, E. Papillon, M. Cotte, P. Walter, and J. Susini, "A multiplatform code for the analysis of energy-dispersive X-ray fluorescence spectra," *Spectrochim. Acta, Part B* **62**(1), 63–68 (2007).
31. A. C. Thompson, J. Kirz, D. T. Attwood, E. M. Gullikson, M. R. Howells, J. B. Kortright, Y. Liu, A. L. Robinson, J. Underwood, K.-J. Kim, I. Lindau, P. Pianetta, H. Winick, G. P. Williams, and J. H. Scofield, "X-Ray Data Booklet," (2009).
32. J. Sherman, "The theoretical derivation of fluorescent {X}-ray intensities from mixtures," *Spectrochim. Acta* **7**, 283–306 (1955).
33. J. W. Criss and L. S. Birks, "Calculation methods for fluorescent x-ray spectrometry. {E}mpirical coefficients versus fundamental parameters," *Anal. Chem.* **40**(7), 1080–1086 (1968).
34. S. D. Rasberry and K. F. J. Heinrich, "Calibration for interelement effects in x-ray fluorescence analysis," *Anal. Chem.* **46**(1), 81–89 (1974).
35. I. Dowding and S. Haufe, "Powerful Statistical Inference for Nested Data Using Sufficient Summary Statistics," *Front. Hum. Neurosci.* **12**, 103 (2018).
36. X. Guan, X. Xu, and M. Zhang, "Region-Specific Iron Measured by MRI as a Biomarker for Parkinson's Disease," *Neurosci. Bull.* **33**(5), 561–567 (2017).
37. K. M. Davies, S. Bohic, A. Carmona, R. Ortega, V. Cottam, D. J. Hare, J. P. M. Finberg, S. Reyes, G. M. Halliday, J. F. B. Mercer, and K. L. Double, "Copper pathology in vulnerable brain regions in Parkinson's disease," *Neurobiol. Aging* **35**(4), 858–866 (2014).
38. M. Szczerbowska-Boruchowska, A. Krygowska-Wajs, and D. Adamek, "Elemental micro-imaging and quantification of human substantia nigra using synchrotron radiation based x-ray fluorescence -in relation to Parkinson's disease," *J. Phys.: Condens. Matter* **24**(24), 244104 (2012).
39. P. F. Good, C. W. Olanow, and D. P. Perl, "Neuromelanin-containing neurons of the substantia nigra accumulate iron and aluminum in Parkinson's disease: a LAMMA study," *Brain Res.* **593**(2), 343–346 (1992).
40. B. F. G. Popescu, M. J. George, U. Bergmann, A. V. Garachtchenko, M. E. Kelly, R. P. E. McCrea, K. Lüning, R. M. Devon, G. N. George, A. D. Hanson, S. M. Harder, L. D. Chapman, I. J. Pickering, and H. Nichol, "Mapping metals in Parkinson's and normal brain using rapid-scanning x-ray fluorescence," *Phys. Med. Biol.* **54**(3), 651–663 (2009).
41. H. Sun, "Association of soil selenium, strontium, and magnesium concentrations with Parkinson's disease mortality rates in the USA," *Environ. Geochem. Health* **40**(1), 349–357 (2018).
42. J. Pánik, M. Kopáni, J. Zeman, M. Jeřkovský, J. Kaizer, and P. P. Povinec, "Determination of metal elements concentrations in human brain tissues using {PIXE} and {EDX} methods," *J. Radioanal. Nucl. Chem.* **318**(3), 2313–2319 (2018).
43. A. Binolfi, R. M. Rasia, C. W. Bertoncini, M. Ceolin, M. Zweckstetter, C. Griesinger, T. M. Jovin, and C. O. Fernández, "Interaction of  $\alpha$ -synuclein with divalent metal ions reveals key differences: A link between structure, binding specificity and fibrillation enhancement," *J. Am. Chem. Soc.* **128**(30), 9893–9901 (2006).
44. Y. Peng, C. Wang, H. Xu, Y.-N. Liu, and F. Zhou, "Binding of  $\alpha$ -Synuclein with Fe(III) and with Fe(II) and Biological Implications of the Resultant Complexes," *J. Inorg. Biochem.* **104**(4), 365–370 (2010).
45. Y. Xiao, X. Chen, S. Huang, G. Li, M. Mo, L. Zhang, C. Chen, W. Guo, M. Zhou, Z. Wu, L. Cen, S. Long, S. Li, X. Yang, S. Qu, Z. Pei, and P. Xu, "Iron promotes  $\alpha$ -synuclein aggregation and transmission by inhibiting TFEB-mediated autophagosome-lysosome fusion," *J. Neurochem.* **145**(1), 34–50 (2018).
46. W. Li, H. Jiang, N. Song, and J. Xie, "Oxidative stress partially contributes to iron-induced alpha-synuclein aggregation in SK-N-SH cells," *Neurotoxic. Res.* **19**(3), 435–442 (2011).
47. J. Levin, T. Högen, A. S. Hillmer, B. Bader, F. Schmidt, F. Kamp, H. A. Kretschmar, K. Bötzel, and A. Giese, "Generation of ferric iron links oxidative stress to  $\alpha$ -synuclein oligomer formation," *J. Parkinson's Dis.* **1**(2), 205–216 (2011).

48. B. Gardner, B. V. Dieriks, S. Cameron, L. H. S. Mendis, C. Turner, R. L. M. Faull, and M. A. Curtis, "Metal concentrations and distributions in the human olfactory bulb in Parkinson's disease," *Sci. Rep.* **7**(1), 1–14 (2017).